Int. J. Heat Mass Transfer. Vol. 34, No. 7, pp. 1823–1838, 1991
Printed in Great Britain

0017-9310/91 $3.00+0.00

Numerical simulation of mixing of coaxial air flows with condensation

X. XU† and V. P. CAREY
Department of Mechanical Engineering, University of California, Berkeley, CA 94720, U.S.A.

(*Received* 19 *June* 1990 *and in final form* 11 *September* 1990)

Abstract—A numerical model is described for the flow and cloud formation processes during co-current mixing of cold dry air and warm moist air in a large-diameter flow chamber. This numerical model solves for the flow pattern and the distributions of temperature, water vapor, and liquid water droplets in the chamber. The computational scheme uses a two-equation turbulence model (k–ε model), which has been modified to include the effects of buoyancy and droplet condensation. The turbulent transport of momentum, heat, species, and droplets are simultaneously determined. The model also incorporates a treatment of the droplet growth and sedimentation mechanisms during the cloud formation process. Samples of the streamlines, isotherms, and contours of constant droplet and species concentrations obtained for a matrix of running conditions are presented. Results from this numerical model indicate that the wall of the cylindrical chamber (oriented vertically) has a very strong influence on the flow field and on the temperature distribution inside the chamber. The model predictions are shown to be in good agreement with limited experimental observations of a coaxial mixing process. The strengths and limitations of the model are also discussed.

1. INTRODUCTION

1.1. *Background*

THE ENVIRONMENTAL impact of man-made aerosols has been an important issue in recent years. An example can be drawn from the so-called 'nuclear winter' phenomenon. Numerical models of global air circulation have been applied to study the climatic effects of the smoke from a possible nuclear war [1–3]. However, accurate prediction of the nuclear winter scenario from the global circulation models depends on, among other things, the nucleation of embryo water droplets on smoke particles. This nucleation process affects the cloud formation and the residence time of the smoke particles in the atmosphere, as noted by Penner *et al.* [4] in a study of the precipitation scavenging of smoke over large fires. Despite their importance, the nucleation properties of different types of smoke particles have not been thoroughly examined.

Recent efforts to experimentally explore the characteristics of smoke particles as condensation nuclei [5, 6] have typically made use of a co-current-flow cloud chamber like that shown in Fig. 1. This type of system provides for the mixing of two coaxial streams, one being a warm, humid, and particle-laden air stream, and the other a cold, dry air stream (Fig. 2). This mixing process produces a region of varying supersaturation in which the excess liquid water content is likely to be condensed on the particles to form droplets. Samples of the interstitial particle fraction (the fraction not inside droplets) and the total particle fraction at the exit are typically collected and analyzed.

Experiments of this type may provide valuable information about the nucleation properties of the aerosol particles. However, to correctly interpret the trends in the data, detailed knowledge of the conditions in the chamber at which nucleation occurs is needed. Detailed information regarding the flow pattern and the distributions of temperature, water vapor, and liquid water droplets in the test chamber

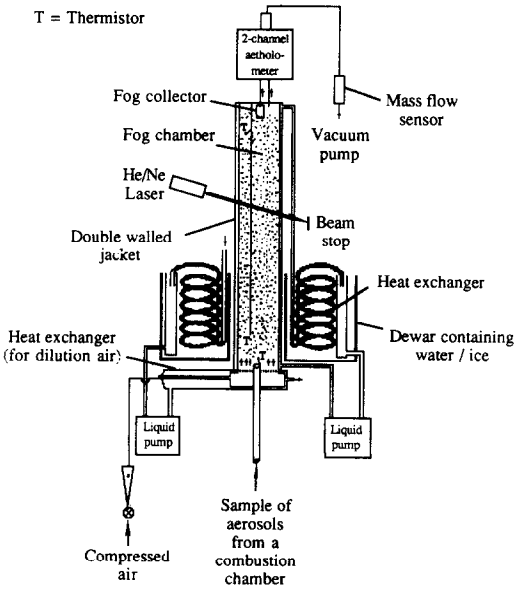

FIG. 1. Schematic of a typical cloud chamber for the study of the nucleation characteristics of smoke particles.

† Present address: Accelerator Division, Superconducting Super Collider Laboratory, Dallas, Texas, U.S.A.

NOMENCLATURE

A, B	parameters in the droplet size distribution formula (equation (19))
C_μ, $C_{1\varepsilon}$, $C_{2\varepsilon}$	empirical constants in k–ε model
c_p	specific heat
D_v	diffusional coefficient of water vapor
E	roughness parameter
G	production of turbulent kinetic energy due to buoyancy
g	gravitational acceleration
h_{fg}	latent heat
k	turbulent kinetic energy
k_a	thermal conductivity of air
m	mass concentration of droplets
m_v	mass concentration of water vapor
N	number concentration of droplets
$n(r)$	size distribution of droplets
P	production of turbulent kinetic energy due to shear stress
P_f	parameter in equation (33)
p	pressure
p_v	vapor pressure
$p_{v,sat}$	vapor pressure at saturation
R	inside radius of mixing chamber
R_f	flux Richardson number
R_w	gas constant of water vapor
r	radial coordinate, droplet radius
S	source term
S_ϕ	source term for scalar variable ϕ in the governing equation (4)
s	humidity ratio
T	temperature
U	mean component of the axial velocity
u	fluctuating component of the axial velocity
u_s	settling velocity of a droplet
V	mean component of the radial velocity
v	fluctuating component of the radial velocity
x	axial coordinate
y	distance between a solid wall and a nearby node.

Non-dimensional parameters

Ct	Craya–Curtet number
Pr	Prandtl number
Re	Reynolds number, UR/ν
Sc	Schmidt number.

Greek symbols

Γ	molecular diffusivity
Γ_{eff}	effective diffusivity, $\Gamma+\Gamma_t$
Γ_t	turbulent diffusivity
ε	rate of dissipation of the turbulent kinetic energy
κ	von Karman constant
λ	Kolmogoroff turbulence length scale
μ	molecular viscosity
μ_{eff}	effective viscosity, $\mu+\mu_t$
μ_t	turbulent viscosity
ν	kinematic viscosity
ρ	fluid density
ρ_v	density of water vapor
ρ_w	density of liquid water
σ_k, σ_ε	empirical constants in k–ε model
σ_ϕ	Prandtl or Schmidt number for variable ϕ
$\sigma_{\phi,t}$	turbulent Prandtl or Schmidt number for variable ϕ
ϕ	any one of the scalar variables (T, s, m or N)
ϕ'	fluctuating component of scalar quantity ϕ
χ	ambient supersaturation
χ_r	equilibrium supersaturation over a droplet surface
ψ	saturation ratio.

is difficult to observe and/or to measure during the experiment. Theoretical predictions of these fields provide an alternative means of exploring the conditions under which cloud formation occurs in the test chamber. A detailed theoretical understanding of the transport conditions also allows researchers to better define the effects of environmental conditions on the nucleation characteristics of the particles.

The study of nucleation properties of aerosols using a co-current-flow cloud chamber is relatively new. As a result, no efforts to computationally model the flow and condensation processes in this type of structure have been found in the literature. There have been experimental and numerical investigations of the turbulent mixing of confined jets in combustors [7–10]. However, the geometric configurations considered in these studies are different from that of the cloud chamber considered here. While studying the concentration fluctuation in the turbulent mixing of coaxial jets, Elghobashi *et al.* [11] considered a geometric configuration similar to that of the cloud chamber shown in Fig. 1. The actual flow pattern in a condensing flow may be very different from that considered by Elghobashi *et al.* [11] because of the additional buoyancy influence and the effects of condensation present in the flow considered here.

1.2. *Objectives of the current study*

This study specifically sought to develop a numerical model of the flow and condensation processes in

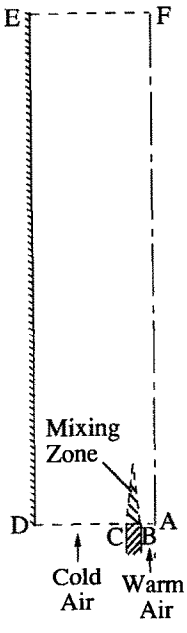

FIG. 2. Schematic diagram of coaxial mixing process.

a co-current-flow cloud chamber so that the effects of convective heat and mass transfer in the flow on droplet nucleation and growth in such circumstances could be better understood. This study was also motivated by a desire to develop a model of the transport that could be used to help define the best experimental conditions for nucleation property determinations, and exploring alternate experimental configurations that could improve the accuracy of data obtained from nucleation experiments.

In this study, the transport equations for the mass, momentum, energy, and the water vapor and droplets as separate species were established. Closure of the scheme also required that we include a turbulence model as well as the effects of buoyancy, droplet sedimentation, droplet growth through condensation, and variations in the droplet size distribution. The well-known TEACH-2E computer program, developed by Gosman and Ideriah [12], was used as a starting point in this investigation. A number of modifications were subsequently made to develop a computation model that accounts for droplet transport, condensation, and heat and mass transfer.

2. DEVELOPMENT OF THE NUMERICAL SCHEME

The problem involved in this study is a multiphase, turbulent, recirculating flow, under the influence of buoyancy and condensation. There are several species in the system: the dry air, the water vapor in the air, and the liquid water droplets formed on the aerosol particles. Due to the complexity of this problem, two idealizations were adopted to simplify the analysis.

First, it was assumed that the presence of the water vapor and the liquid water droplets has a negligible impact on the flow field since the volumetric concentration of these components in the mixture is very small. During the cloud chamber experiments at LBL, the measured mass concentration of the cloud droplets was in the range of 1–3 g m^{-3}, corresponding to a volume fraction of 10^{-6}–3×10^{-6}.

Secondly, it was assumed that the presence of the liquid water droplets in the test chamber has no effect on the turbulence structure. For the test conditions considered here, the average droplet radius r is less than 10 μm and the volumetric concentration of droplets is usually very low. Moreover, the estimated dissipation rate of the turbulent kinetic energy, ε, is of the order of 10^{-3}–1 (because the Reynolds number of the flow is about 10^2–10^3 [13]). By definition, the Kolmogoroff length scale $\lambda = (\nu^3/\varepsilon)^{1/4}$ is estimated to be in the range 200–1000 μm. Hence, $r \ll \lambda$, implying that the droplet size is much less than the length scale that characterizes the smallest turbulence eddies, and the droplet concentration is generally very low. The effect of the drops on damping of turbulence is expected to be small. As a first approximation, we therefore neglected such effects in this study, and treated the droplets as a passive scalar transported by the turbulence.

2.1. *Transport equations for turbulent flow*

For steady, incompressible, axisymmetric flow, the equations of continuity and momentum for the mean quantities are (see ref. [14])

$$\frac{\partial U}{\partial x}+\frac{1}{r}\frac{\partial V}{\partial r}=0 \tag{1}$$

$$\rho\left(U\frac{\partial U}{\partial x}+V\frac{\partial U}{\partial r}\right)=-\frac{\partial p}{\partial x}+\frac{\partial}{\partial x}\left(2\mu_{\text{eff}}\frac{\partial U}{\partial x}\right)+\frac{1}{r}\frac{\partial}{\partial r}\left(r\mu_{\text{eff}}\left(\frac{\partial U}{\partial r}+\frac{\partial V}{\partial x}\right)\right)+g(\rho-\rho_{\text{m}}) \tag{2}$$

$$\rho\left(U\frac{\partial V}{\partial x}+V\frac{\partial V}{\partial r}\right)=-\frac{\partial p}{\partial x}+\frac{\partial}{\partial x}\left(\mu_{\text{eff}}\left(\frac{\partial V}{\partial x}+\frac{\partial U}{\partial r}\right)\right)+\frac{1}{r}\frac{\partial}{\partial r}\left(2r\mu_{\text{eff}}\frac{\partial V}{\partial r}\right)-2\mu_{\text{eff}}\frac{V}{r^2} \tag{3}$$

where p is the pressure, ρ the fluid density, g the gravitational acceleration in the axial direction. The parameter μ_{eff} is the effective viscosity defined as $\mu_{\text{eff}}=\mu+\mu_{\text{t}}$, where μ is the molecular viscosity and μ_{t} the eddy viscosity.

The governing equations for the mean scalar quantities such as temperature, T, humidity ratio, s, the total mass concentration of the droplets, m, and the total number concentration of the droplets, N, can be expressed as

$$\rho\left(U\frac{\partial\phi}{\partial x}+V\frac{\partial\phi}{\partial r}\right)=\frac{\partial}{\partial x}\left(\Gamma_{\text{eff}}\frac{\partial\phi}{\partial x}\right)+\frac{1}{r}\frac{\partial}{\partial r}\left(r\Gamma_{\text{eff}}\frac{\partial\phi}{\partial r}\right)+S_\phi \tag{4}$$

where ϕ stands for any one of the scalar variables (T, s, m or N), and S_ϕ is the corresponding source term. Γ_{eff} is the effective diffusivity

$$\Gamma_{\text{eff}} = \Gamma + \Gamma_t = \frac{\mu}{\sigma_\phi} + \frac{\mu_t}{\sigma_{\phi,t}} \tag{5}$$

where σ_ϕ is the Prandtl or Schmidt number and $\sigma_{\phi,t}$ the turbulent Prandtl or Schmidt number. It is assumed that $\sigma_{\phi,t} = 1$ for all ϕ.

In the study described here, the well-known k–ε turbulence model (see, for example, Lauder and Spalding [15]) was used, k being the kinetic energy of turbulence and ε the rate of dissipation of k. In the k–ε model, the eddy viscosity μ_t is given by

$$\mu_t = C_\mu \rho \frac{k^2}{\varepsilon}. \tag{6}$$

The governing equations for k and ε in cylindrical coordinates are given by [16]

$$\rho\left(U\frac{\partial k}{\partial x} + V\frac{\partial k}{\partial r}\right) = \frac{\partial}{\partial x}\left[\frac{\mu_t}{\sigma_k}\frac{\partial k}{\partial x}\right] + \frac{1}{r}\frac{\partial}{\partial r}\left[\frac{\mu_t}{\sigma_k} r \frac{\partial k}{\partial r}\right] + (P+G) - \rho\varepsilon \tag{7}$$

$$\rho\left(U\frac{\partial \varepsilon}{\partial x} + V\frac{\partial \varepsilon}{\partial r}\right) = \frac{\partial}{\partial x}\left[\frac{\mu_t}{\sigma_\varepsilon}\frac{\partial \varepsilon}{\partial x}\right] + \frac{1}{r}\frac{\partial}{\partial r}\left[\frac{\mu_t}{\sigma_\varepsilon} r \frac{\partial \varepsilon}{\partial r}\right] + C_{1\varepsilon}\frac{\varepsilon}{k}(P+G)(1+C_{3\varepsilon}R_f) - C_{2\varepsilon}\rho\frac{\varepsilon^2}{k} \tag{8}$$

where P and G represent the production of k by the shear stresses and by buoyancy, respectively

$$P = \mu_t\left\{2\left[\left(\frac{\partial U}{\partial x}\right)^2 + \left(\frac{\partial V}{\partial r}\right)^2 + \left(\frac{V}{r}\right)^2\right] + \left(\frac{\partial U}{\partial r} + \frac{\partial V}{\partial x}\right)^2\right\} \tag{9}$$

$$G = \beta g \frac{\mu_t}{\sigma_{T,t}}\frac{\partial T}{\partial x}. \tag{10}$$

Values of the empirical constants C_μ, $C_{1\varepsilon}$, $C_{2\varepsilon}$, σ_k and σ_ε have been optimized for many internal and external flows. The most frequently used values of these constants are listed in Table 1. They were used here without modification. R_f in equation (8) is called the flux Richardson number [16]

$$R_f = -\frac{1}{2}\frac{G_{\overline{v^2}}}{P+G} \tag{11}$$

where $G_{\overline{v^2}}$ is the buoyancy production of the lateral fluctuating component $\overline{v^2}$. For the vertical flow encountered in this study, R_f is equal to zero.

To solve equations (1)–(8), the source term in equation (4), S_ϕ, needs to be determined. In order to formulate S_ϕ in equation (4), it is necessary to consider the mechanisms of droplet growth and sedimentation during the condensation process around the aerosol particles. These aerosols act as cloud condensation nuclei (CCN) on which the available excess moisture in the air collects to form liquid water droplets.

Table 1. The empirical constants used in the k–ε model

$C_\mu = 0.09$,	$C_{1\varepsilon} = 1.44$,	$C_{2\varepsilon} = 1.92$,	$\sigma_k = 1.0$,	$\sigma_\varepsilon = 1.3$

2.2. *Modeling of droplet growth due to condensation*

For the total mass concentration of the droplets, m, the source term S_m can be written as

$$S_m = \rho\left(\left[\frac{\partial m}{\partial t}\right]_{\text{grow}} + \left[\frac{\partial m}{\partial t}\right]_{\text{sedi}} + \left[\frac{\partial m}{\partial t}\right]_{\text{coag}}\right) \tag{12}$$

where the three terms on the right-hand side represent the three mechanisms in the cloud formation process—growth, sedimentation, and coagulation [17]. The growth term represents the growth of droplets due to condensation of water vapor that diffuses to the surface of the droplet. The sedimentation term represents the gravity-induced motion of droplets relative to the main stream, and the coagulation term represents the collision between droplets.

As mentioned earlier, the estimated average drop radius r is less than 10 μm. In experimental studies [18], the number concentration of the droplets was visually observed to be in the range of 1000–8000 cm^{-3}, which indicates that the average distance between the droplets is around 0.5–1 mm. Because the drops are far apart compared to their size, the coagulation term in equation (12) was neglected.

The rate of condensation for each droplet is dictated by its size and the local temperature and humidity conditions. The size and number of the droplets were characterized by a size distribution function. Assuming that the droplets were spherical with radius r, the size distribution function, $n(r)$, was defined by

$$\mathrm{d}N = n(r)\,\mathrm{d}r \tag{13}$$

where $\mathrm{d}N$ is the number concentration of droplets in the droplet radius range r to $r+\mathrm{d}r$. From the definition, the total number and mass concentration of droplets are computed as

$$N = \int_0^\infty n(r)\,\mathrm{d}r, \quad m = \int_0^\infty \rho_w\left(\tfrac{4}{3}\pi r^3\right)n(r)\,\mathrm{d}r. \tag{14}$$

The effect of condensation on the total mass and number concentrations was obtained by integrating the effect for the individual size groups over the entire size spectrum. For instance, the growth term in equation (12)

$$\left[\frac{\partial m}{\partial t}\right]_{\text{grow}} = \int_0^\infty \left[\frac{\partial m}{\partial t}\right]_{r,\text{grow}} n(r)\,\mathrm{d}r \tag{15}$$

where $[\partial m/\partial t]_{r,\text{grow}}$ denotes the rate of change of drop mass, due to growth, for a droplet with radius r.

The growth of an individual droplet due to con-

densation has been studied by several researchers [19, 20]. We adopted the formula derived by Fitzgerald [19] for the initial stages of cloud droplet condensation, because the conditions for which it was developed are very close to those in our investigation. The relation describing the droplet rate of growth is

$$r\frac{\mathrm{d}r}{\mathrm{d}t} = F(T,p)(\chi-\chi_r) \tag{16}$$

where

$$\chi = \frac{p_{\mathrm{v},\infty}}{p_{\mathrm{v,sat}}(T_\infty)} - 1$$

is the ambient fractional supersaturation and

$$\chi_r = \frac{A'}{r} - \frac{B'}{r^3}$$

is termed the equilibrium supersaturation over the droplet surface. The term A' represents the surface curvature effect and the term B' accounts for the effect of chemical composition (dissolved salt). The definitions of A' and B' can be found in ref. [19]. In general, A' and B' are small when the drop radius is larger than 1 μm and when the salt in the drop is sufficiently diluted. They are assumed to be zero in this study, which implies that $\chi_r = 0$. The term $F(T,p)$ in equation (16) is given by

$$F(T,p) = \frac{1}{\rho_{\mathrm{w}}\left(\dfrac{R_{\mathrm{w}}T}{D_{\mathrm{v}}p_{\mathrm{v,sat}}(T)} + \dfrac{L^2}{k_{\mathrm{a}}R_{\mathrm{w}}T^2}\right)} \tag{17}$$

where $p_{\mathrm{v,sat}}(T)$ is the vapor pressure under saturation conditions, D_{v} the diffusivity of water vapor, k_{a} the thermal conductivity of moist air, L the latent heat, ρ_{w} the density of liquid water, and R_{w} the gas constant of water vapor.

From equation (16), it follows that

$$\left[\frac{\partial m}{\partial t}\right]_{r,\mathrm{grow}} = \rho_{\mathrm{w}}\frac{\mathrm{d}}{\mathrm{d}t}(\tfrac{4}{3}\pi r^3) = \rho_{\mathrm{w}}4\pi r F(T,p)\chi. \tag{18}$$

Note that the growth model used here (embodied in equations (16)–(18)) allows droplets to grow for $p_{\mathrm{v},\infty} > p_{\mathrm{v,sat}}(T)$ or shrink if $p_{\mathrm{v},\infty} < p_{\mathrm{v,sat}}(T)$. As seen in equation (15), $n(r)$ also needs to be specified before we can compute $[\partial m/\partial t]_{\mathrm{grow}}$. For cloud droplets, a so-called Khrgian–Mazin size distribution has often been postulated (see ref. [20]). This distribution takes the form

$$n(r) = Ar^2\exp(-Br) \tag{19}$$

where A and B are coefficients that vary depending on conditions. From equations (14) and (19) m and N can be calculated as functions of A and B.

Equations (15) and (18) can be combined to obtain the source term for the total droplet mass concentration due to growth

$$\left[\frac{\partial m}{\partial t}\right]_{\mathrm{grow}} = \int_0^\infty \rho_{\mathrm{w}}4\pi r F(T,p)\chi n(r)\,\mathrm{d}r. \tag{20}$$

We subsequently consider the sedimentation term in equation (12). If the radius of the droplet is smaller than 10 μm (as considered here), this downward flow is in the Stokes flow regime, and the resulting relative velocity (which is usually called the settling velocity) can be derived as

$$u_{\mathrm{s}} = \frac{2\rho_{\mathrm{w}}r^2 g}{9\mu}. \tag{21}$$

The part of the source term S_m due to sedimentation, therefore, is given by

$$\left[\frac{\partial m}{\partial t}\right]_{\mathrm{sedi}} = \frac{\partial}{\partial x}\int_0^\infty u_{\mathrm{s}}\rho_{\mathrm{w}}(\tfrac{4}{3}\pi r^3)\,\mathrm{d}N = \frac{\partial}{\partial x}\int_0^\infty u_{\mathrm{s}}\rho_{\mathrm{w}}(\tfrac{4}{3}\pi r^3)n(r)\,\mathrm{d}r. \tag{22}$$

The source term for m can then be expressed as

$$S_m = \rho\left(\left[\frac{\partial m}{\partial t}\right]_{\mathrm{grow}} + \left[\frac{\partial m}{\partial t}\right]_{\mathrm{sedi}}\right). \tag{23}$$

As for the total number concentration of the droplets, it is assumed here that condensation occurs only at the existing aerosol particles. The particles were assumed to be fully wetted. Consequently, droplets grow on all particles. For such conditions, N will not be affected by the growth mechanism

$$S_N = \rho\left[\frac{\partial N}{\partial t}\right]_{\mathrm{sedi}}. \tag{24}$$

The right-hand side can be calculated by

$$\left[\frac{\partial N}{\partial t}\right]_{\mathrm{sedi}} = \frac{\partial}{\partial x}\int_0^\infty u_{\mathrm{s}}\,\mathrm{d}N = \frac{\partial}{\partial x}\int_0^\infty u_{\mathrm{s}}n(r)\,\mathrm{d}r. \tag{25}$$

The source term for the energy equation is

$$S_T = -\frac{1}{c_p}\left[\frac{\partial q}{\partial t}\right] = \frac{h_{\mathrm{fg}}}{c_p}\left[\frac{\partial m}{\partial t}\right]_{\mathrm{grow}}. \tag{26}$$

In the equation for the humidity ratio, s, evaluation of the source term is based on the conservation of mass for the water specie. The amount of water vapor lost is equal to the amount of liquid water gained by droplets due to condensation

$$\left[\frac{\partial m_{\mathrm{v}}}{\partial t}\right] = -\left[\frac{\partial m}{\partial t}\right]_{\mathrm{grow}}. \tag{27}$$

It follows from the definition of s, $s = m_{\mathrm{v}}/\rho_{\mathrm{air}} \approx m_{\mathrm{v}}/\rho$, that

$$S_s = \rho\left[\frac{\partial s}{\partial t}\right] = \rho\left[\frac{\partial m_{\mathrm{v}}/\rho}{\partial t}\right] = -\left[\frac{\partial m}{\partial t}\right]_{\mathrm{grow}} \tag{28}$$

where m_{v} is the mass concentration of the water vapor and ρ_{air} the density of the dry air. Equations (23), (24),

(26) and (28) thus provide the source terms for the energy equation and the species equations.

2.3. *Boundary conditions*

To solve the elliptic governing equations, boundary conditions must be specified on all of the boundaries of the flow domain, shown as ABCDEF in Fig. 2. The variables U, V, T, s, m and N are assigned values at AB and CD. Following the practice of Gosman and Ideriah [12], k and ε are computed from $k = 0.03U^2$ and $\varepsilon = k^{1.5}/l$, respectively, where l is the length scale of turbulence and is assumed to be 0.005 times the radius of the pipe, R. At the axis of symmetry, AF, the radial gradients of all the variables are equal to zero. And at the exit plane, EF, it is assumed that the fully developed flow conditions have been achieved.

At a wall boundary, wall functions are used to connect the wall boundary condition to the fully turbulent region. The law-of-the-wall is applied here for the momentum equation

$$\frac{U_p}{U_\tau} = \frac{1}{\kappa}\ln(Ey_p^+) \tag{29}$$

where the subscript p designates the grid node closest to the wall, U_p the velocity parallel to the wall at this node, $U_\tau = \sqrt{(\tau_w/\rho)}$ the friction velocity, $y_p^+ = y_p U_\tau/\nu$ the dimensionless wall distance of node p, κ the von Karman constant, and E a roughness parameter ($E = 9.973$ is recommended in ref. [12] and is applied here). In the k–ε model, an inertial sublayer is usually assumed to exist where the shear stress is nearly constant and local equilibrium prevails, and the production of k is balanced by its rate of dissipation (convection and diffusion of k are neglected). From this practice, the shear stress in the inertial sublayer, τ_w, can be related to k and the turbulence constants

$$\tau_w = \rho C_\mu^{1/2} k_p. \tag{30}$$

This relation is normally used as the boundary condition for k. The boundary condition for ε can also be derived as

$$\varepsilon_p = C_\mu^{3/4}\frac{k_p^{3/2}}{\kappa y_p}. \tag{31}$$

Equations (29)–(31) provide the boundary conditions for the momentum equations and k and ε equations.

A similar wall function for the energy equation, relating the heat flux at the wall to the difference between the wall temperature, $T_w(x)$, and the temperature in the inner region, is also presented in ref. [12]. From ref. [12], the local heat flux was related to the temperature at node p by

$$T_p = T_w - \frac{q_w'' Pr_t}{\rho C_p U_\tau}\left(\frac{U_p}{U_\tau} + P_j\right) \tag{32}$$

where the function P_j is given by

$$P_j = 9.24\left[\left(\frac{Pr}{Pr_t}\right)^{0.75} - 1\right]. \tag{33}$$

For the passively transported species, zero gradients normal to the wall are often applied as the proper wall boundary conditions. The wall functions therefore are unnecessary for the species variables.

2.4. *Computational technique*

The TEACH-2E code, developed by Gosman and Ideriah [12], was modified to account for the additional mechanisms associated with the droplet condensation process.

Grid-independent results were obtained using a 36×24 non-uniform grid (36 nodes in the axial direction and 24 nodes in the radial direction). A finer grid (72×24) was found to result in a 1% difference in the velocity and temperature profiles compared with the 36×24 grid for conditions typical of the flows of interest here. Since the finer grid required considerably more computer storage and computing time, and offered no significant increase in accuracy, the 36×24 grid was used for most of the calculations.

The under-relaxation factors ranging from 0.3 to 0.7 were used in most of the cases in our study. Convergence is assumed to be achieved when the maximum residue sources of all the equations is less than a threshold (in this study, assigned to 0.001 times the fixed flux of the relevant variable at the inlet plane).

Most of the computations were carried out on a Digital DEC 3100 workstation. Generally, it required 3000–4000 iterations to obtain the converged solution for a typical case, taking about 200 min of CPU time. For the testing cases in which the effects of buoyancy and condensation were not included, 600–1000 iterations are required to obtain a converged solution.

3. DISCUSSION OF THE RESULTS

The numerically obtained results from the finite-difference computer code are presented in this section. Several benchmark cases are discussed first. Then, the streamlines, isothermals, and the constant contours of the species concentrations for a typical running condition are plotted and described in detail. A number of parametric studies also are discussed.

3.1. *Benchmark cases*

In order to verify that the computer program was functioning correctly, several test runs were first conducted. Each is discussed in turn next.

3.1.1. *Simple pipe flow.* Where the velocities of the coaxial jets entering the pipe channel are identical and the jets are isothermal, the flow pattern becomes that of a pipe-flow case. For this case, the results in the fully-developed region are obtained from our computer code by neglecting the buoyancy and droplet condensation terms. These results are shown in Table

2, where they are compared with the experimental measurements of Laufer [21] and with the numerical predictions of Elghobashi *et al.* [11]. The Reynolds number is 5×10^5. In Table 2, y represents the distance from the pipe wall; R is the pipe radius, U the axial velocity, k the turbulent kinetic energy, ε the dissipation rate of k, and τ_w the wall shear stress. It can be seen that good agreement has been achieved, especially for the velocity distribution.

3.1.2. *Coaxial jets without buoyancy.* In another benchmark case, the finite-difference code was run for the situations in which the buoyancy term was not included, because experimental results were available for these situations [22]. For a fixed geometry, a recirculation zone appears near the pipe wall when the ratio of the central-jet velocity to the surrounding jet velocity exceeds a certain value (Fig. 3). The flow pattern for such a situation can be characterized by the locations of the separation and reattachment points. In their experimental study, Becker *et al.* [22] measured these positions and correlated the measurements with a parameter, Ct, called the Craya–Curtet number

$$Ct = U_0/\sqrt{((U_1^2 - U_2^2)(r/R)^2 + 0.5(U_2^2 - U_0^2))} \qquad (34)$$

where

$$U_0 = (U_1 - U_2)(r/R)^2 + U_2.$$

Figure 4 shows the variation of the separation and reattachment locations with Ct, measured by Becker *et al.* [22] and predicted by our numerical model. Also shown are the numerical predictions of Elghobashi *et al.* [11]. As can be seen, our predictions show the right trend, and the agreement with the measured data is reasonably good, although the separation locations are a little under-estimated and the reattachment locations a little over-estimated in our model.

3.1.3. *Comparison of the predicted and measured temperature distribution.* Differences between the situations encountered in the cloud chamber experiments and those described in the previous sections are largely a result of buoyancy effects due to the temperature difference between the inlet warm and cold air jets and the temperature difference between the chamber wall and the adjacent air stream. These extra characteristics of the real flow during the experiment resulted in significant changes in the flow pattern and the temperature distribution.

For one running condition, the temperature distribution inside a cloud chamber has been obtained from the experimental measurements [18]. These results are shown in Fig. 5(a). We therefore further evaluated our numerical model by comparing our predicted temperature distribution for this running condition to the measured one.

The inlet conditions for this run are

$$U_1 = 0.45\,\mathrm{m\,s^{-1}}, \quad U_2 = 0.011\,\mathrm{m\,s^{-1}}$$

$$T_1 = 39^\circ\mathrm{C}, \qquad T_2 = -25.8^\circ\mathrm{C}.$$

Table 2. Comparison of the numerical predictions and experimental results for pipe flow. $Re = 5 \times 10^5$

y/R	U/U_{max}			$k/(\tau_s/\rho)$			$\varepsilon R/(\tau_s/\rho)^{1.5}$		
	Our predictions	Experiment Laufer [21]	Predictions Elghobashi *et al.* [11]	Our predictions	Experiment Laufer [21]	Predictions Elghobashi *et al.* [11]	Our predictions	Experiment Laufer [21]	Predictions Elghobashi *et al.* [11]
0.1	0.787	0.78	0.776	3.03	3.70	3.33	24.9	22.0	22.9
0.2	0.856	0.85	0.848	2.68	2.90	2.87	11.9	11.5	12.1
0.3	0.898	0.89	0.889	2.37	2.50	2.50	7.24	7.5	7.47
0.4	0.930	0.92	0.924	2.08	2.10	2.18	4.86	6.5	4.99
0.5	0.953	0.95	0.949	1.82	1.90	1.90	3.42	5.0	3.49
0.6	0.971	0.97	0.968	1.60	1.40	1.67	2.48	3.5	2.53
0.7	0.984	0.98	0.983	1.41	1.20	1.49	1.86	3.0	1.89
0.8	0.993	0.99	0.992	1.27	1.10	1.35	1.47	2.6	1.51
0.9	0.998	1.0	0.998	1.19	0.9	1.28	1.25	2.5	1.29
1.0	1.00	1.0	1.00	1.16	0.9	1.25	1.18	2.4	1.23

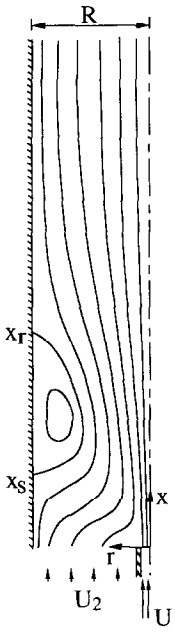

FIG. 3. Streamlines for the flow situation without buoyancy.

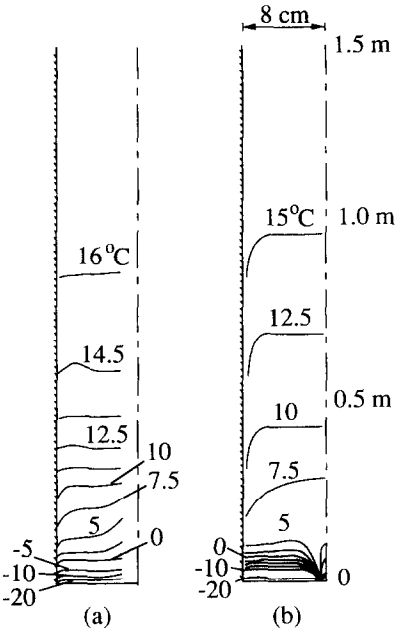

FIG. 5. Comparison of the experimentally measured (a) and the numerically predicted (b) isotherms.

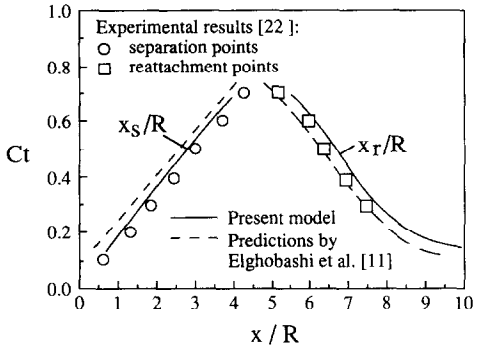

FIG. 4. Variation of the separation and reattachment locations with the Craya–Curtet number for the flow situation without buoyancy.

Unfortunately, the temperature along the chamber wall was not measured in the experiment, and the exact boundary conditions for the temperature equation are not known. The wall temperature profile was therefore obtained by extrapolating the temperature measurements [18] inside the chamber. We subsequently curvefit the extrapolated wall temperature values with the following relations which were then used to predict the wall boundary condition in our computations for these experimental conditions:

$$\begin{aligned} T_w(^\circ\mathrm{C}) &= -14.58+3x, && x = 0\text{–}6\,\mathrm{cm} \\ &\quad 1.2+0.37x, && 6\text{–}30\,\mathrm{cm} \\ &\quad 10.5+0.06x, && 30\text{–}100\,\mathrm{cm} \\ &\quad 16.5, && 100\text{–}50\,\mathrm{cm}. \end{aligned} \quad (35)$$

The numerically predicted isotherms are displayed in Fig. 5(b). Relatively satisfactory agreement can be seen between the experimental results and our predictions. At the location 0.5 m downstream of the entrance, the measured temperature is around 13.5°C, while the predicted temperature is around 10°C. The locations of the 5°C isotherm in these three figures are even closer, although the shapes of the measured and predicted results start to differ in the region where $r < 3$ cm (r is the radial coordinate).

It should be noted, however, that the flow pattern and the temperature distribution could be somewhat disturbed by the presence of the thermistors used to measure the temperatures during the experiment, making it almost impossible to precisely compare the numerical predictions with the measurements. Hence, the agreement between the predictions and the measurements appears to be within the expected uncertainty in the data.

3.2. *A typical running condition for nucleation studies*

In this section, results from the full model (i.e. including the model of droplet condensation) are presented for a typical running condition encountered in the experiment. The corresponding inlet conditions are listed in Table 3.

In Table 3, subscripts 1 and 2 represent, respec-

Table 3. The inlet conditions and wall temperature for the typical case

$U_1 = 0.9\ \mathrm{m\,s^{-1}}$,	$U_2 = 0.011\ \mathrm{m\,s^{-1}}$
$T_1 = 49.7^\circ\mathrm{C}$,	$T_2 = -20^\circ\mathrm{C}$
$s_1 = 0.0692$ ($T_d = 46^\circ\mathrm{C}$),	$s_2 = 0$
$m_1 = 100\ \mu\mathrm{g\,m^{-3}}$,	$m_2 = 0$
$N_1 = 50\,000\ \mathrm{cm^{-3}}$,	$N_2 = 0$
$T_w(x) = 0.85x\ (^\circ\mathrm{C})$, $x < 16.5$ cm	
$14.0\ (^\circ\mathrm{C})$, $x \geq 16.5$ cm	

tively, the values for the warm air and the cold air jet at the inlet. T_w denotes the wall temperature profile, and T_d the dew point of the warm air. The $T_w(x)$ used here is assumed, since no measured data are available. The number concentration of the aerosol particles at the inlet, N_1, is also assumed. Hence, the numerical results presented here provide only qualitative assessment of the real process. The numerically obtained streamlines, isothermals, and the constant contours of the saturation ratio, the mass and number concentrations of the droplets for this case are discussed in the next four sections.

3.2.1. *Streamlines.* Figure 6 displays the streamlines for the typical running condition. A first recirculation zone is observed in the flow near the inlet end of the side wall due to entrainment of the outer flow into the central jet. It can also be seen that the central jet begins to flow towards the wall at 20–30 cm downstream of the inlet, because the temperature difference between the wall and the nearby air stream induces a strong upward buoyancy influence which brings about entrainment towards the wall. As a result, a second recirculation zone appears near the centerline due to the entrainment of the centerline core flow into the upward buoyancy-driven boundary-layer flow near the wall. This buoyancy effect diminishes at further downstream locations ($x \sim 80$ cm) as the thermal energy of the wall diffuses to the inner region and the mean temperature of the fluid rises. The flow is fully developed beyond $x = 100$ cm.

Also, because of the buoyancy-induced entrainment of the central jet towards the wall, the recirculation zone near the wall is confined to a region 5–20 cm downstream of the entrance (see Fig. 6). As a result, the cold surrounding jet at the bottom of the chamber ($x \sim 0$–4 cm) flows almost horizontally towards the centerline, resulting in the nearly horizontal streamlines in this region.

3.2.2. *Isotherms.* The isotherms for the typical running condition are shown in Fig. 7. It can be seen that the highest temperature gradients exist in the mixing layer between the two jets ($r \sim 0$–1 cm, $x \sim 0$–10 cm). In a distance of only about 10 cm, the temperature of the central warm jet decreases rapidly from 49.7 to 10°C, while the temperature of the annular cold jet increases from −20 to 7.5°C. Near the inlet, the entrainment of the annular jet towards the centerline resulted in the nearly flat isotherms in that area.

The recirculation zones provide vigorous sites for thermal mixing, so that the temperature gradients are small in these zones. From Figs. 6 and 7, it can easily be seen that the central portion of the 12.5°C isothermal, located in the upper recirculation zone, is flat, indicating that the temperature gradient in the radial direction in that region is zero. The thermal developing region near the wall is apparent at $x \sim 25$ cm, just above the lower recirculation zone. At this location, the temperature gradient is relatively large. For example, at $x \sim 30$ cm, the temperature decreases from 14 to 12.5°C within about 3 mm from the wall. Further downstream along the wall, the temperature drops less rapidly as the thermal boundary layer develops.

3.2.3. *Saturation ratio and the cloud region.* The saturation ratio, ψ, is the ratio of the partial pressure of the water vapor to that pressure at the saturation condition. ψ can be expressed as $\psi = \chi + 1$, where χ is the supersaturation of the air. As shown in the droplet growth model (equation (16)), condensation will

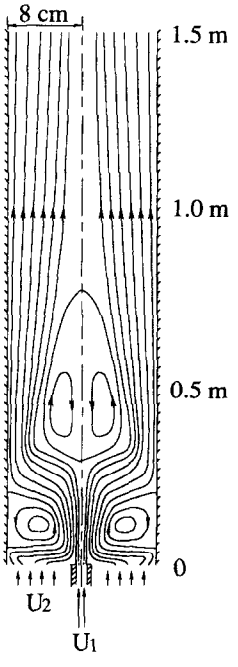

FIG. 6. Streamlines for a typical running condition. $U_1 = 0.9$ m s^{-1}, $U_2 = 0.011$ m s^{-1}.

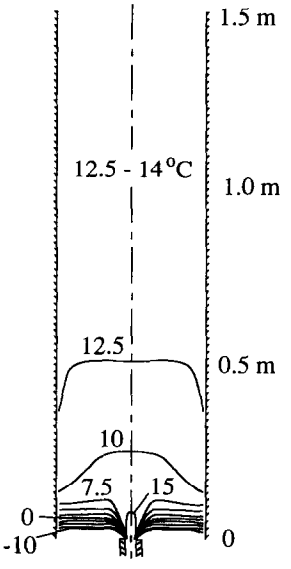

FIG. 7. Isotherms for a typical running condition. The temperature of the central warm air is 49.7°C, and that of the annular cold air is −20°C.

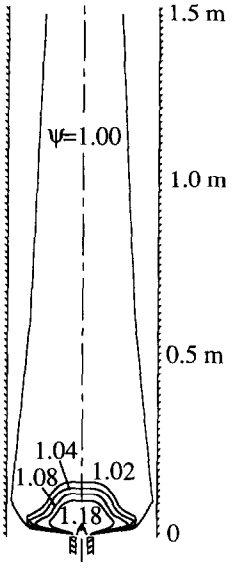

FIG. 8. Contours of constant saturation ratio for a typical running condition. The dew point of the central warm air is 46°C.

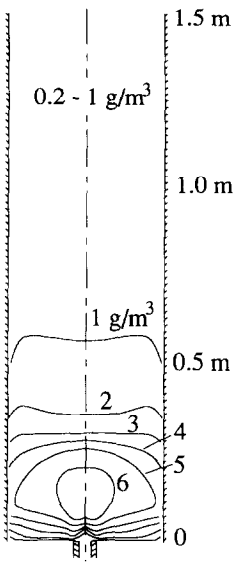

FIG. 9. Contours of constant droplet mass concentration for a typical running condition.

occur when $\chi > \chi_r$, where χ_r is the equilibrium supersaturation over the droplet surface. Since χ_r is assumed to be zero in this study, the cloud forms when $\chi > 0$ (or $\Psi > 1$).

Figure 8 shows the contours of constant saturation ratio. For the typical running condition, where $T_d = 46°C$, $\psi = 1$ in the region beyond 20 cm from the entrance, except in the near-wall region where ψ is a few percent less than one. However, cloud droplets are also present in this near-wall region because the droplets are also transported by convection and diffusion mechanisms, some of which have not yet completely evaporated.

In the mixing region ($r \sim 1$ cm, i.e. 1 cm from the centerline) near the inlet, the numerical results indicate that the supersaturation can be as high as 350% (at $x \sim 1$ cm). The equilibrium condition in this mixing layer is difficult to achieve because of the steep gradients. At $x \sim 5$ cm, the supersaturation is still around 50%. It decreases from 20% at $x \sim 10$ cm to 0 at $x \sim 20$ cm. In addition, strong variation of the saturation ratio with radius can be seen in the annular jet region near the entrance.

3.2.4. *Concentrations of liquid droplets and the size distribution.* The formation of droplets can be seen from the distribution of the droplet mass and number concentrations, m and N. Figures 9 and 10 display the constant contours of these concentrations.

In Fig. 9, it can be seen that m is largest near the centerline at 10–20 cm from the entrance. It is interesting to examine the effect of the flow pattern, especially the recirculation zones, on the distribution of the droplet mass concentration. Since the downward velocity in the recirculation zones enhances the sedimentation, droplets tend to accumulate under these recirculation regions. The relatively large m in the annular jet region near the bottom of the chamber illustrates this tendency. The region of high droplet mass concentration around the centerline, as mentioned before, is another example.

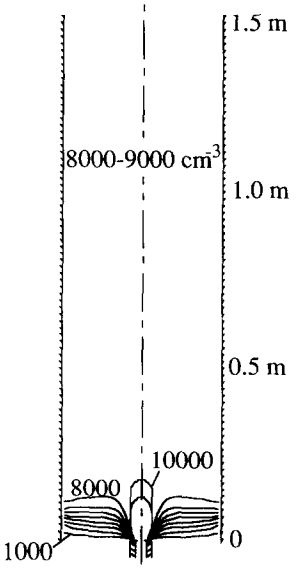

FIG. 10. Contours of constant droplet number concentration for a typical running condition. The number concentration of the aerosol particles in the central warm air is 50 000 cm^{-3}.

During the experiment, the measured drop mass concentration at the middle of the test chamber ($x \sim 70$ cm) normally was about 1–3 g m^{-3} [18]. The numerically predicted m for the typical case is about 1 g m^{-3} at $x \sim 70$ cm. Because m is very sensitive to the mean temperature of the saturated air (m will increase significantly if the mean temperature of the air is slightly decreased), and because the mean tem-

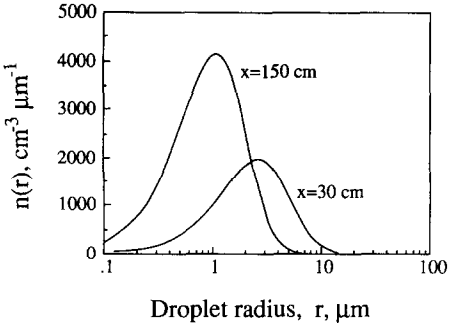

FIG. 11. The size distributions of cloud droplets at two downstream locations along the centerline, $x = 30$ and 150 cm, for a typical running condition. There is no cloud at the inlet ($x = 0$). The aerosol particles at the inlet were postulated to have a uniform radius of 0.08 μm and a number concentration of 50 000 cm^{-3}.

perature of the air is related to the wall temperature, thus, allowing for the fact that we have used an approximated wall temperature profile, our predicted m in this region agrees quite well with the experimental measurements.

In Fig. 10, it can be seen that the variation of drop number concentration is very small for $x > 10$ cm. Also, at the bottom of the chamber the shapes of the N contours are very similar to the shapes of the isothermals (Fig. 7). Both N and T are dominated by the convection and diffusion mechanisms. Hence, in areas where the influence of the wall boundary is small, the distributions of N and T ought to be similar. In addition, the effect of sedimentation on the distribution of N is believed to be small, since only the large droplets which account for a small portion of the entire droplet population (N) are likely to precipitate. It should be mentioned that homogeneous nucleation and droplet coagulation are neglected in our model. Although these effects are expected to be small, neglecting them may introduce some additional inaccuracy in the predicted results.

Based on the numerically obtained m and N, the size distribution of the cloud drops $n(r)$, at any location in the chamber can be calculated using equation (16). Figure 11 shows the computed size distribution of the drops for cloud parcels at two locations along the axis of symmetry, $x = 30$ and 150 cm (exit). It can be seen that the peak of $n(r)$ at $x = 150$ cm occurs at smaller droplet radius than the peak of $n(r)$ at $x = 30$ cm, reflecting the fact that drops are generally smaller at $x = 150$ cm than at $x = 30$ cm.

3.3. *Parametric study: variation of the inlet conditions*

In order to assess the effect of varying the inlet conditions, several parametric studies are performed. Two parameters, the dew point, and the number concentration of aerosol particles at the inlet, were examined. The rest of the inlet conditions and the wall temperature profile are the same as those of the typical running condition, listed in Table 3.

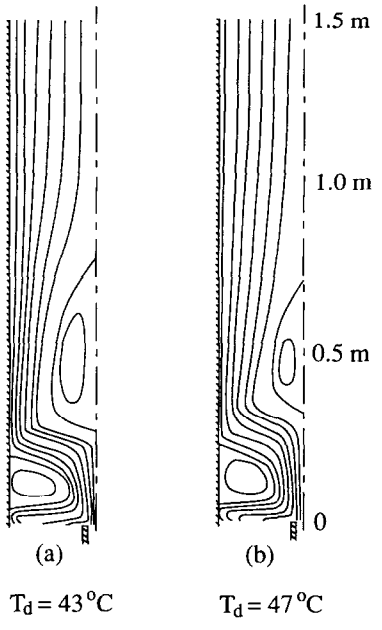

FIG. 12. Comparison of the streamlines for different values of the dew point of the central warm air at the inlet.

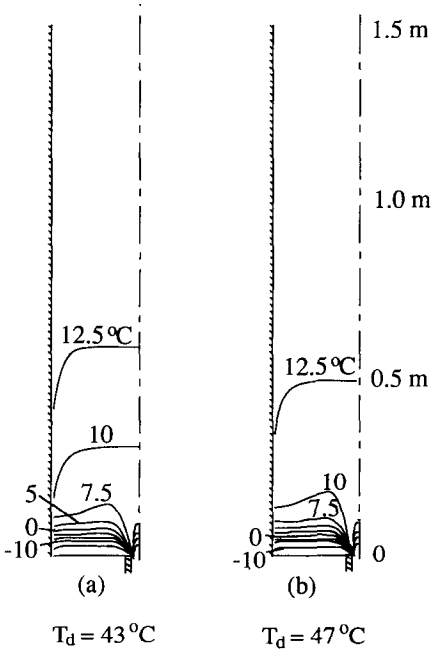

FIG. 13. Comparison of the isotherms for different values of the dew point of the central warm air at the inlet.

3.3.1. *Variation of the dew point of the central air jet.* The effect of varying the dew point at the inlet can be seen in Figs. 12–16, where comparisons are made between the results for $T_d = 43$ and 47°C, which correspond to $\psi = 70.6$ and 86.7% when the temperature of warm air at the inlet is $T_i = 49.7$°C.

Figure 12 shows the computed streamlines for these two cases. The flow pattern is changed only slightly by

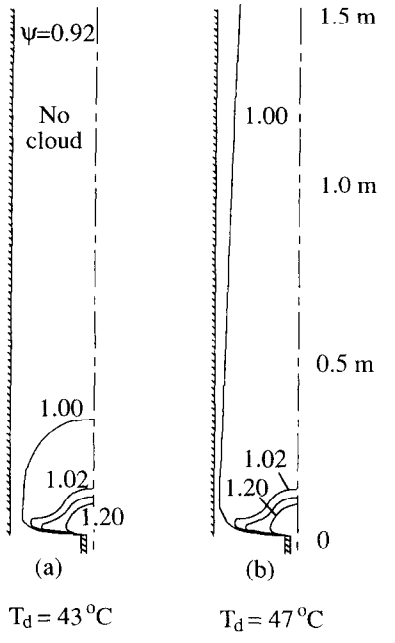

FIG. 14. Comparison of the contours of constant saturation ratio for different values of the dew point of the central warm air at the inlet. (Edge of cloud is expected to correspond to $\psi = 1.0$.)

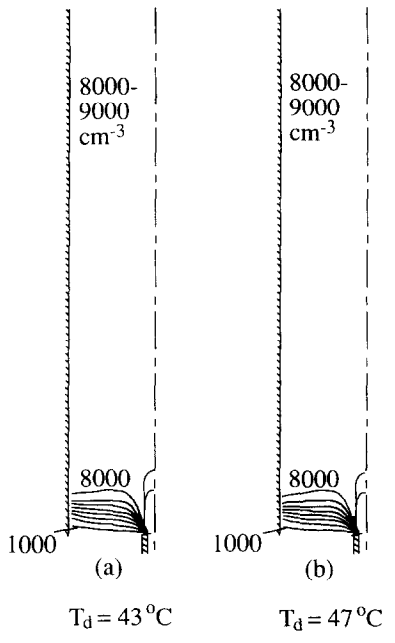

FIG. 16. Comparison of the contours of constant droplet number concentration for different values of the dew point of the central warm air at the inlet.

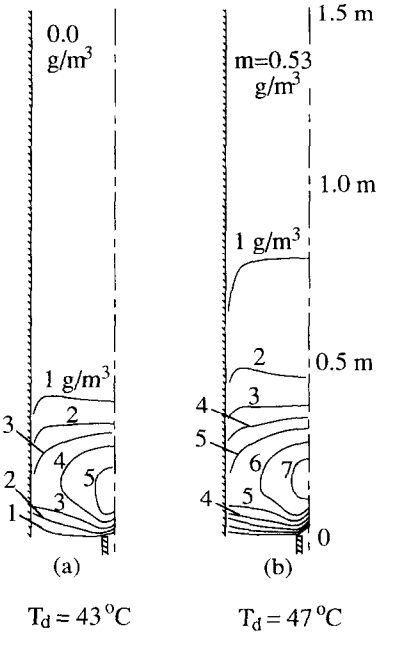

FIG. 15. Comparison of the contours of constant droplet mass concentration for different values of the dew point of the central warm air at the inlet.

varying T_d. The central recirculation region becomes smaller as T_d increases. Because more water vapor is injected into the chamber as T_d increases, the latent heat released during the condensation process increases. As a result, the thermal mixing near the wall is accelerated, thus reducing the buoyancy force near the wall and attracting less flow towards the near-wall region. This also appears to explain the variation of the isotherms in these two cases (see Fig. 13) which indicates that higher temperatures are achieved earlier in the chamber when the inlet T_d is higher.

As shown in Fig. 14, the cloud area is very sensitive to the dew point. When the inlet dew point is 43°C, the region where $\psi \geqslant 1$ (ψ is the saturation ratio) occupies only the lower part of the chamber, reaching $x \sim 30$ cm. While for $T_d = 47$°C, the $\psi \geqslant 1$ region occupies almost the entire chamber. Beyond the saturation condition, a small increase in dew point results in a relatively large amount of excess moisture.

Figure 15 displays the mass concentrations of drops at these two dew points. At the same location in the lower part of the chamber, m is higher when T_d is higher. However, at the upper half of the chamber, variation of m is only marginal. This is because more excess water condensing on the limited number of available aerosols only gives rise to larger drops on average. The large drops gather at the bottom region of the chamber as a result of sedimentation.

The distributions of N are shown in Fig. 16. It can be seen that N was not affected much by the variation in T_d. Because precipitation would only affect the large drops, the total number should not be greatly affected.

3.3.2. *Variation of the number concentration of aerosols at inlet.* The effect of the inlet aerosol number variation is discussed in this section. Since the cold air stream is chilled, relatively clean ambient air, the only source of aerosol particles is the warm air. Because we assume that condensation occurs on all the aerosol

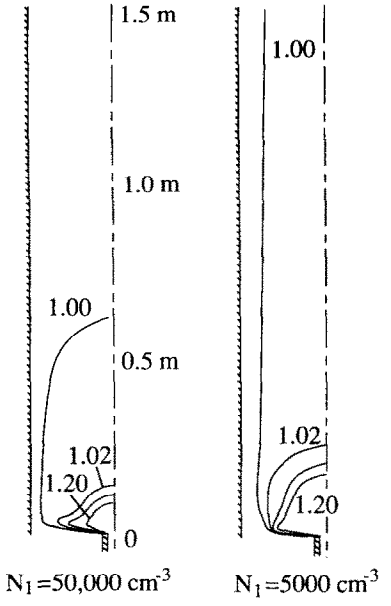

FIG. 17. Comparison of the contours of constant saturation ratio for different values of the particle number concentration in the central warm air at the inlet.

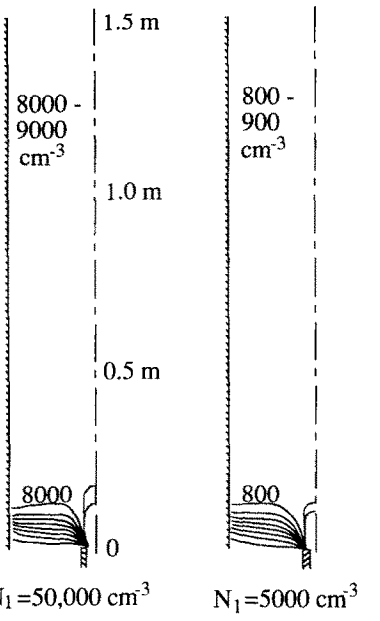

FIG. 19. Comparison of the contours of constant droplet number concentration for different values of the particle number concentration in the central warm air at the inlet.

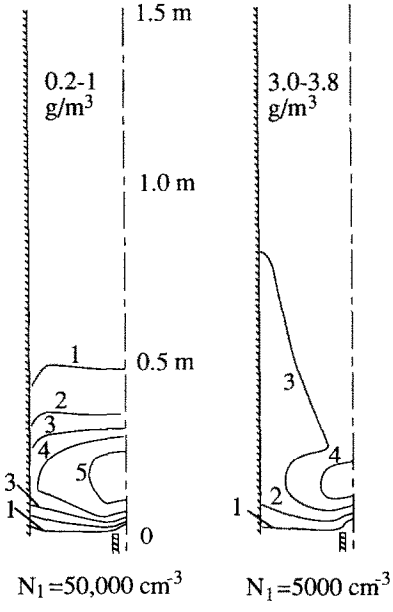

FIG. 18. Comparison of the contours of constant droplet mass concentration for different values of the particle number concentration in the central warm air at the inlet.

particles (i.e. all the particles are CCN), at the same dew point, a smaller number of injected aerosol particles results in larger drops on average. Figures 17–19 show the results for two inlet aerosol number concentrations, $N_1 = 5000$ and 50 000 cm^{-3}. The dew point value of 44°C is used for both cases. The rest of the inlet conditions are the same as those listed in Table 3.

The flow pattern and the temperature distribution are not affected much by the variation in N_1. Hence, the computed streamlines and the isotherms for these conditions are not shown. The saturation ratios are shown in Fig. 17. At the same location near the bottom of the chamber ($x < 25$ cm), the supersaturation is higher in the case $N_1 = 5000$ cm^{-3} than in the case $N_1 = 50\,000$ cm^{-3}. For example, at $x = 10$ cm on the centerline, the supersaturation is about 20% when $N_1 = 5000$ cm^{-3}, and it is about 70% when $N_1 = 50\,000$ cm^{-3}. Furthermore, cloud covers almost the entire chamber when $N_1 = 5000$ cm^{-3}, while it only covers the lower part of the chamber when $N_1 = 50\,000$ cm^{-3}.

The most noticeable effect of varing N_1 is shown by the distribution of droplet mass concentration (Fig. 18). In the upper portion of the chamber ($x > 50$ cm), m is equal to 3.0–3.8 g m^{-3} in the case where $N_1 = 5000$ cm^{-3}, much bigger than for $N_1 = 50\,000$ cm^{-3} where m is equal to 0.2 ~ 1 g m^{-3}. This indicates that the average droplet size in the upper part of the chamber is largest in the case $N_1 = 5000$ cm^{-3} than in the case $N_1 = 50\,000$ cm^{-3} (due to the larger m and smaller N). If these drops are not big enough to cause precipitation (i.e. $u_s < U$), the residence time for the relatively bigger droplets may be longer due to the smaller differences between U and u_s. (For the case of $N_1 = 5000$ cm^{-3}, $u_s \sim 0.7$ cm s^{-1} in the upper part of the chamber, based on $m \sim 3.5$ g m^{-3} and $N \sim 900$ cm^{-3}, while U, the velocity of the main stream, is about 1 cm s^{-1}). Hence, the total amount of droplet mass remaining in the chamber may be larger in the case $N_1 = 5000$ cm^{-3} than in the case $N_1 = 50\,000$ cm^{-3}.

The constant contours for N are very similar in

shape for these two cases, as shown in Fig. 19. It can be seen that at the same location the values of N for both cases are almost in proportion.

4. CONCLUSIONS

In this study, a computational scheme has been developed to simulate the flow and cloud formation processes in the coaxial mixing of a cold dry air flow with a hot moist jet. This mixing process is typical of cloud chambers that have been designed to examine the nucleation properties of aerosol particles [5, 6]. Our numerically obtained flow field and distributions of temperature and the concentrations of water droplets provide interesting theoretical insight into the cloud formation processes in a test chamber of this type. The parametric studies based on the numerical model could offer the prospect of defining the best experimental conditions for nucleation property determinations.

Several conclusions can be reached from the computational results:

(1) For one running condition, comparisons of the numerically predicted isothermals to the experimentally measured ones demonstrated satisfactory agreement. This suggests that the droplet growth and transport models and the turbulence closure scheme used in our computational model are appropriate, at least as first approximations, for flows of this type. However, more detailed comparisons of the model predictions with experimental data are desirable to fully validate the model.

(2) In addition to the recirculation zone near the wall usually observed in the case of isothermal coaxial jet flows in a duct for a certain range of the Craya–Curtet number, the buoyancy effect induced by the wall temperature variation results in a second recirculating zone next to the centerline.

(3) The entrainment of the central jet into the upward buoyancy-driven flow along the wall of the chamber confines the first recirculation zone to the region 0.05–0.2 m from the bottom of the chamber. Thus the annular jet flows nearly horizontally in the area below the first recirculation zone, as demonstrated by the streamlines in that area in Fig. 10. The flat isothermals in that region are a direct consequence of this feature of the flow pattern (Fig. 11).

(4) The largest droplet mass concentration is predicted to exist near the centerline at 10–20 cm from the entrance, just below the central recirculation zone. Since the downward velocity in the recirculation regions enhances the sedimentation, droplets tend to accumulate under these recirculation regions. For the assumed number concentration of aerosol particles at the inlet ($N_1 = 50\,000$ cm^{-3}), the obtained droplet number concentration ranges from 8000 to 9000 cm^{-3} in the upper portion of the cloud chamber.

In spite of the apparent success of this computational method, it is clear that several aspects of the model could be improved. One is that the flow in the chamber is typically a low Reynolds number (100–900) turbulent flow, while the common k–ε turbulence model used in high Reynolds number flow situations was applied here. To extend the turbulence models to the near-wall and low-Reynolds-number flows, a number of so-called low-Reynolds-number turbulence models have been developed in recent years. Generally, these models add a damping factor to the turbulent viscosity, μ_t, as described in a review by Patel *et al.* [23]. Models of this type may be somewhat better suited to these flow circumstances.

The modeling of the condensation process is also somewhat idealized in this study. The properties and the size distributions of the smoke particles are assumed. Coagulation is neglected, and the settling velocity formula only applies to those droplets the radii of which are less than 10 μm. Moreover, the boundary conditions specified at the wall of the chamber may not accurately represent the real situation. For example, condensation on the wall has been observed during some experiments [18]. To completely correct these deficiencies remains a formidable task.

While the model developed in this investigation is approximate in many ways, it nevertheless provides considerable insight into the nature of the cloud formation process in a mixing flow test chamber for particle nucleation studies. At the same time, our results indicate that more work, along the lines described above, is needed to fully understand the physics of cloud formation processes in mixing flows of the type considered here.

Acknowledgements—Support for this research was provided by the National Science Foundation under research grant No. CBT-8451781 and by Lawrence Livermore Laboratory under grant No. LLNL-IGPP-89-08.

REFERENCES

1. C. Covey, S. A. Thompson and S. H. Schneider, Nuclear winter: a diagnosis of atmospheric general circulation model simulations, *J. Geophys. Res.* **90,** 5615–5628 (1985).
2. S. L. Thompson, Global interactive transport simulations of nuclear war smoke, *Nature* **317,** 35–39 (1985).
3. I. Colbeck and R. M. Harrison, The atmospheric effects of nuclear war—a review, *Atmos. Environ.* **20,** 1673–1681 (1986).
4. J. E. Penner, L. C. Haselman, Jr. and L. L. Edwards, Smoke-plume distributions above large-scale fires: implications for simulation of nuclear winter, *J. Climate Appl. Meterology* **23,** 1434–1444 (1986).
5. W. H. Benner, A. D. A. Hansen and T. Novakov, A concurrent-flow cloud chamber study of incorporation of black carbon into droplets, *Aerosol Sci. Technol.* **10,** 84–92 (1989).
6. A. D. A. Hansen and T. Novakov, Cloud chamber studies of the nucleation characteristics of smoke particles from liquid-fuel and wood fires, in preparation.
7. F. K. Owen, Measurement and observations of turbulent recirculating jet flows, *AIAA J.* **14,** 1556–1562 (1976).
8. M. Nallasamy, Computation of confined turbulent coaxial jet flows, *J. Propulsion* **3,** 263–268 (1987).
9. M. A. Habib and J. H. Whitelaw, Velocity characteristics

of a confined coaxial jet, *J. Fluids Engng* **101**, 521–529 (1979).
10. G. Ilic, D. Milojevic and D. Voronjec, On the thermal, dynamic and turbulent development of the heated confined jet, *Proc. Eighth Int. Heat Transfer Conf.*, San Francisco, California, Vol. 3, pp. 1159–1163 (1986).
11. S. E. Elghobashi, W. M. Pun and D. B. Spalding, Concentration fluctuations in isothermal turbulent confined coaxial jets, *Chem. Engng Sci.* **32**, 161–166 (1977).
12. A. D. Gosman and F. J. K. Ideriah, TEACH-2E: a general computer program for two-dimensional, turbulent, recirculating flows, Department of Mechanical Engineering, Imperial College, London (1976).
13. H. Tennekes and J. L. Lumley, *A First Course in Turbulence*, Chap. 1. MIT Press, Cambridge, Massachusetts (1972).
14. S. Dosanjh and J. A. C. Humphrey, The influence of turbulence on erosion by a particle-laden fluid jet, *Wear* **102**, 309–330 (1983).
15. B. E. Lauder and D. B. Spalding, *Lectures in Mathematical Models of Turbulence*. Academic Press, London (1972).
16. W. Rodi, *Turbulence Models and their Application in Hydraulics—a State of the Art Review*. IAHR, Delft, The Netherlands (1984).
17. S. K. Friedlander, *Smoke, Dust, and Haze: Fundamentals of Aerosol Behavior*. Wiley, New York (1977).
18. A. D. Hansen, W. H. Benner and T. Novakov, Private communication (1989).
19. J. W. Fitzgerald, A study of the initial phase of cloud droplet growth by condensation: comparison between theory and observation, Ph.D. Thesis, Chicago University (1972).
20. H. R. Pruppacher and J. D. Klett, *Microphysics of Clouds and Precipitation*. D. Reidel, Dordrecht, The Netherlands (1978).
21. J. Laufer, Structure of turbulence in fully developed pipe flow, NACA Report 1174 (1953).
22. H. A. Becker, H. C. Hottel and G. C. Williams, Concentration intermittency in jets, *Tenth Symp. on Combustion*, pp. 1253–1263 (1965).
23. V. C. Patel, W. Rodi and G. Scheuerer, Turbulence models for near-wall and low Reynolds numbers flows: a review, *AIAA J.* **23**, 1308–1319 (1985).

SIMULATION NUMERIQUE DU MELANGE D'ECOULEMENTS D'AIR COAXIAUX AVEC CONDENSATION

Résumé—On décrit un modèle numérique pour l'écoulement et les mécanismes de formation de nuage pendant le mélange cocourant d'un air sec et froid et d'un air chaud et humide dans une enceinte de grand diamètre. Ce modèle donne la configuration de l'écoulement et les distributions de température, de vapeur d'eau et de gouttelettes liquide d'eau dans la chambre. On utilise pour cela un modèle de turbulence (k–ε) modifié pour inclure les effets de flottement et de condensation en gouttelettes. On détermine simultanément le transport turbulent de quantité de mouvement, de chaleur, d'espèce et de gouttelettes. Le modèle contient un traitement de croissance de gouttelettes et de mécanisme de sédimentation pendant la formation du nuage. On présente des exemples de lignes de courant, d'isothermes, de contours de concentration constante de gouttelettes et d'espèces pour une matrice de conditions opératoires. On trouve que la paroi de la chambre cylindrique (orientée verticalement) a une très forte influence sur le champ de vitesse et sur la distribution de température dans la chambre. Les prédictions sont en bon accord avec les quelques observations expérimentales sur le mécanisme de mélange coaxial. On discute aussi des avantages et des limitations du modèle.

NUMERISCHE SIMULATION DER MISCHUNG ZWEIER KOAXIALER LUFTSTRÖME MIT KONDENSATION

Zusammenfassung—Es wird ein numerisches Modell beschrieben, das zur Berechnung der Strömung und der Wolkenbildung bei der Mischung kalter trockener Luft mit warmer feuchter Luft im Gleichstrom in einer Strömungskammer mit großem Durchmesser dient. Das numerische Modell beschreibt das Strömungsfeld sowie die Verteilungen von Temperatur, Wasserdampf und flüssigen Wassertröpfchen in der Kammer. Es wird ein höheres k–ε-Turbulenzmodell verwendet, das zur Berücksichtigung von Auftriebseffekten und Tröpfchenkondensation erweitert worden ist. Der turbulente Impuls-, Wärme-, Massen- und Tröpfchentransport wird simultan bestimmt. Das Modell umfaßt außerdem die Behandlung der Mechanismen von Tropfenwachstum und Tropfensedimentation während des Vorgangs der Wolkenbildung. Für eine Matrix von Berechnungsvorgaben werden die Stromlinien, die Isothermen sowie die Linien konstanter Tröpfchen—bzw. Massenkonzentration dargestellt. Die Ergebnisse dieses numerischen Modells zeigen, daß die Wand der zylindrischen Kammer (senkrecht ausgerichtet) einen sehr starken Einfluß auf das Strömungsfeld und die Temperaturverteilung in der Kammer hat. Die Aussagen des Modells stimmen gut mit den begrenzt vorhandenen experimentellen Untersuchungen des koaxialen Mischungsprozesses überein. Abschließend werden die Stärken und die Grenzen des Modells diskutiert.

ЧИСЛЕННОЕ МОДЕЛИРОВАНИЕ СМЕШЕНИЯ КОАКСИАЛЬНЫХ ПОТОКОВ ВОЗДУХА ПРИ НАЛИЧИИ КОНДЕНСАЦИИ

Аннотация—Описывается численная модель процессов течения и образования облаков при спутном смешении ненагретого сухого и нагретого влажного воздуха в камере течения с большим диаметром. Предложенная численная модель позволяет определить картину течения, а также распределения температуры, воденого пара и капель воды в камере. В вычислительной схеме используется двухпараметрическая модель турбулентности (k–ε модель), модифицированная для учета эффектов подъемной силы и капельной конденсации. Одновременно определяется турбулентный перенос импульса, тепла, пара и капель. Модель также описывает механизмы роста и осаждения капель в процессе образования облаков. Приводится образцы линий тока, изотерм и линий постоянных концентраций капель и вещества для матрицы варьируемых условий. Результаты, полученные на основе численной модели, свидетельствуют о том, что стенка цилиндрической камеры (направленной вертикально) оказывает значительное влияние на поле течения и распределение температур в камере. Показано, что расчеты, сделанные с использованием модели, хорошо согласуются с немногими экспериментальными наблюдениями над процессом коаксиального смешения. Обсуждаются также достоинства и недостатки предложенной модели.